

Pyramid diffractive optical networks for unidirectional magnification and demagnification

Bijie Bai^{1,2,3}, Xilin Yang^{1,2,3}, Tianyi Gan^{1,3}, Jingxi Li^{1,2,3}, Deniz Mengu^{1,2,3}, Mona Jarrahi^{1,3}, and Aydogan Ozcan^{*,1,2,3}

¹Electrical and Computer Engineering Department, University of California, Los Angeles, CA, 90095, USA.

²Bioengineering Department, University of California, Los Angeles, 90095, USA.

³California NanoSystems Institute (CNSI), University of California, Los Angeles, CA, USA.

*Correspondence: Aydogan Ozcan. Email: ozcan@ucla.edu

Abstract

Diffraction deep neural networks (D²NNs) are composed of successive transmissive layers optimized using supervised deep learning to all-optically implement various computational tasks between an input and output field-of-view (FOV). Here, we present a pyramid-structured diffractive optical network design (which we term P-D²NN), optimized specifically for unidirectional image magnification and demagnification. In this P-D²NN design, the diffractive layers are pyramidally scaled in alignment with the direction of the image magnification or demagnification. Our analyses revealed the efficacy of this P-D²NN design in unidirectional image magnification and demagnification tasks, producing high-fidelity magnified or demagnified images in only one direction, while inhibiting the image formation in the opposite direction – confirming the desired unidirectional imaging operation. Compared to the conventional D²NN designs with uniform-sized successive diffractive layers, P-D²NN design achieves similar performance in unidirectional magnification tasks using only half of the diffractive degrees of freedom within the optical processor volume. Furthermore, it maintains its unidirectional image magnification/demagnification functionality across a large band of illumination wavelengths despite being trained with a single illumination wavelength. With this pyramidal architecture, we also designed a wavelength-multiplexed diffractive network, where a unidirectional magnifier and a unidirectional demagnifier operate *simultaneously* in opposite directions, at two distinct illumination wavelengths. The efficacy of the P-D²NN architecture was also validated experimentally using monochromatic terahertz illumination, successfully matching our numerical simulations. P-D²NN offers a physics-inspired strategy for designing task-specific visual processors.

Introduction

The fusion of machine learning techniques and optics/photonics has fostered unprecedented breakthroughs in recent years, bridging the gap between traditional computational methods and the promising avenues of optical processing¹⁻³. With the recent advances in data-driven artificial intelligence design methodologies, optical computing platforms have gained design complexity with new capabilities, providing transformative solutions for various computational tasks⁴⁻⁹. These optical computing and visual processing platforms utilize the unique characteristics of light, such as phase, spectrum and polarization, to rapidly process optical information, offering advantages of parallel processing, computational speed, and energy efficiency. In this line of research, diffractive deep neural networks (D²NNs) have emerged as a free-space optical platform that leverages supervised deep learning algorithms to design diffractive surfaces for visual processing and all-optical computational tasks^{10,11}. These diffractive optical networks, after their fabrication, form physical all-optical processors of visual information, capable of executing various computer vision tasks, spanning image classification^{10,12-15}, quantitative phase imaging (QPI)^{16,17}, linear transformations¹⁸⁻²¹, image encryption²²⁻²⁴, and imaging through diffusive media^{25,26}, among many others²⁷⁻³⁴. The visual processing and optical computing capabilities of D²NNs hinge on the modulation of light diffraction through a sequence of spatially structured and optimized diffractive surfaces. Within the modulation area of each diffractive layer, there exist hundreds of thousands or more light modulation units with a lateral feature size of $\sim\lambda/2$, forming the diffractive neurons/features of the optical network, which represent the independent degrees of freedom of the visual processor, collectively modulating the amplitude and phase of the transmitted light fields. Complex-valued transmission coefficients of these diffractive layers are optimized using deep learning algorithms, and once optimized and fabricated, a D²NN completes its computational task at the speed of light propagation through passive light diffraction through a thin volume, making it a powerful tool for visual processing tasks.

Here, we present a pyramid-structured diffractive network design and demonstrate its utility for unidirectional image magnification and demagnification tasks. In this pyramid diffractive network design (termed P-D²NN), the size of the successive diffractive layers, and consequently, the number of diffractive neurons/features on each layer, scale in alignment with the desired magnification or demagnification factor. Therefore, the size of the initial diffractive layer is proportional to the size of the input object field-of-view (FOV), while the size of the terminal diffractive layer aligns with the size of the output FOV – following a desired magnification or demagnification operation. Intermediate diffractive layers are proportionally scaled to geometrically align with the evolving fields during light propagation within the diffractive network (Figs. 1b-c). Based on this geometrical optics-inspired P-D²NN architecture, we demonstrated unidirectional image magnification and demagnification tasks: when the incident light

propagates along one pre-determined direction, the diffractive network magnifies (or demagnifies) the images from its corresponding input FOV and generates the magnified (or demagnified) images at the output FOV. On the other hand, when the incident light propagates along the opposite direction, the diffractive network inhibits image formation, generating very low-intensity and unrecognizable weak images at the output FOV (Figs. 1b-c). We evaluated the effectiveness of the P-D²NN architecture by comparing it against the conventional D²NN designs with uniformly-sized diffractive layers. Our results indicate that the P-D²NN can achieve a comparable level of unidirectional image magnification performance as the regular D²NN architecture – but uses only half of the diffractive features/neurons due to its tapered geometry. Our P-D²NN-based unidirectional magnifier/demagnifier designs maintain the designed functionality under a broader range of illumination wavelengths, even though they are trained using a single illumination wavelength. We also designed a wavelength-multiplexed P-D²NN that simultaneously performs *unidirectional magnification* at one wavelength of operation, while performing *unidirectional demagnification* at another wavelength in the opposite direction, further demonstrating the design versatility of the presented system.

We also experimentally verified the efficacy of our P-D²NN framework using monochromatic terahertz (THz) illumination. After its deep learning-based optimization, the resulting diffractive layers were fabricated using 3D printing and assembled to be tested under continuous-wave THz illumination at $\lambda = 0.75$ mm. The experimentally measured results closely align with our numerical simulations, where the output images at the image magnification direction accurately reflect the magnified versions of the input images, while the outputs in the opposite direction produce low-intensity, non-informative results.

Using significantly less numbers of diffractive features, this physics-inspired pyramid diffractive optical network design framework would be useful for creating compact visual processing systems, potentially mitigating data overfitting and reducing fabrication costs in visual processing systems.

Results

P-D²NN for unidirectional image magnification and demagnification

Throughout this study, we consistently refer to the optical path from field-of-view (FOV) A to FOV B as the forward direction, and the reversed path as the backward direction (see Fig. 1a). We first demonstrate unidirectional magnification using a spatially coherent pyramid diffractive optical network, as illustrated in Fig. 1b. In this optical system, when the incident light propagates along the forward direction, the diffractive network magnifies the input images from FOV A and generates the corresponding magnified

output images at FOV B. However, as a *unidirectional* magnification system, the opposite path functions differently. When images at FOV B propagate along the backward direction, the diffractive network inhibits the image formation at FOV A by scattering the optical fields outside of the output FOV, therefore resulting in very low-intensity and unrecognizable output images at FOV A – as desired in a unidirectional imaging design.

As shown in Fig. 2a, the pyramid network used for unidirectional magnification contains five diffractive layers with progressively increasing numbers of diffractive features on each layer. These diffractive features on each surface have a characteristic size of approximately half the wavelength of the illumination light, which modulate the phase of the transmitted optical field by introducing an optical path length difference at the diffraction limit of light. Outside the effective areas of the diffractive layers that contain these phase modulation features, the regions at the edges are set as non-transmissive, completely blocking the light field that reaches these edge regions of a diffractive layer. This P-D²NN architecture is designed to achieve a geometrical image magnification factor of $M = 3$ in the forward direction, transitioning from an input FOV (FOV A) of 90×90 pixels to an output FOV (FOV B) of 270×270 pixels. In this configuration, the size of the progressively increasing diffractive layers are set to 90×90 , 140×140 , 180×180 , 220×220 , and 270×270 pixels (diffractive features), respectively, leading to a total number of $N = N_b = 181,400$ trainable diffractive neurons. The axial spacing between consecutive layers was set to $\sim 53.3\lambda$. Based on this geometric configuration, the pyramid diffractive network was first digitally modeled, and the modulation depths of all diffractive features were iteratively optimized using deep learning (see the Methods section). The optimization target was driven by minimizing a set of custom-designed loss functions that enable unidirectional magnification, designed to achieve three primary objectives: (1) maximizing the structural similarity between the output images in the forward direction ($A \rightarrow B$) and the corresponding ground truth images (i.e., the magnified versions of the input images) using normalized mean square error (NMSE) and the negative Pearson Correlation Coefficient (PCC)³⁵; (2) enhancing the diffraction efficiency in the forward direction ($A \rightarrow B$); and (3) suppressing the diffraction efficiency in the backward direction ($B \rightarrow A$). Further details of the network architecture and the mathematical formulation of the loss functions can be found in the Methods section. Utilizing this customized loss function, the optimization of the diffractive layers was carried out via a data-driven supervised training process using the images from the QuickDraw dataset³⁶ supplemented by an additional image dataset with grating/fringe-like patterns^{17,29}. By tuning the weighting coefficient (i.e., energy boost factor β) of the customized loss term designed for enhancing the diffraction efficiency in the forward direction ($A \rightarrow B$), the diffractive networks were successfully trained to simultaneously achieve high-quality image magnification and a decent diffraction efficiency in the forward direction (see Figs.

2c-d). In our quantitative performance analyses, we trained six independent models with the same P-D²NN architecture using different β values. These models were subsequently tested on a separate dataset of 1600 test images which were not seen during the training phase. The performance of each trained P-D²NNs was quantified based on several metrics: (1) PCC between the output and the corresponding ground truth images in the forward direction ($A \rightarrow B$); (2) PCC between the output and original images in the backward direction ($B \rightarrow A$); (3) diffraction efficiency in the forward direction; (4) diffraction efficiency in the backward direction; and (5) the energy ratio between the forward and backward output images (see the Methods section). For example, Fig. 2b illustrates the diffractive layers of a converged P-D²NN trained using $\beta = 1$, whose blind test results are demonstrated in Fig. 2c. The quantitative metrics listed above were calculated for all β settings, as summarized in Fig. 2d. For the $\beta = 1$ case, it is observed that the trained P-D²NN exhibits an asymmetric behavior, as desired, where the output images at the forward direction closely resemble the magnified input images with a PCC value as high as 0.934, and a forward diffraction efficiency of 20.4% (dashed lines in Fig. 2d). In contrast, the backward path only retains a diffraction efficiency of 0.05%, resulting in very low-intensity images with a backward PCC as low as 0.144 (Fig. 2d). This diffractive network, in its unidirectional magnification task, achieves an average energy suppression ratio of ~ 46 -fold between the backward and the forward directions.

Additional quantitative assessments across all six models with different β values (Fig. 2d) reveal that increasing β further boosts the forward diffraction efficiency. However, this enhancement is coupled with a decrease in the forward PCC and a slight increase in the backward PCC. The diffraction efficiency in the backward direction also increases slowly with the larger β values. As shown in Fig. 2d, the forward-backward energy ratio is first improved and then slowly drops beyond $\beta = 1.5$. Visualization of blind testing image examples for different β values can be found in Supplementary Fig. S1. These quantitative analyses and comparisons reveal that there are various design choices available that can adjust the P-D²NN design to achieve a desirable range of forward diffraction efficiency and unidirectional image magnification quality, while also significantly suppressing the backward PCC and diffraction efficiency (see Fig. 2d).

Following a similar design method, we also performed *unidirectional demagnification* through a pyramid diffractive network with decreasing layer sizes along the forward light propagation direction, as illustrated in Fig. 1c. This diffractive network shrinks the input images at FOV A, yielding demagnified output images at FOV B along the forward path. Based on its unidirectional imaging design, in the backward direction, the network inhibits the image formation from FOV B to FOV A and produces very weak and unrecognizable output images. Similar to the magnification P-D²NN, this P-D²NN design for unidirectional demagnification comprises five diffractive layers, each containing progressively smaller

number of diffractive features that modulate the phase of the transmitted optical fields (Fig. 3a). We selected a demagnification factor of $D = 3$ in the forward direction, shrinking an input image of 270×270 pixels down to an output image of 90×90 pixels. The axial spacing between successive diffractive layers is kept the same as before, $\sim 53.3\lambda$. The optimization process of the diffractive layers follows the same methodology as the unidirectional magnification models reported in Fig. 2, where the same set of loss functions and training data were used (see the Methods section). The same quantitative analysis was also performed for the unidirectional demagnification P-D²NN using six unique models which were numerically trained under different energy boost factors β , and blindly tested using 1600 test images not included in the training phase, as summarized in Figs. 3b-d.

Figure 3b shows the diffractive layers of a converged P-D²NN model designed with $\beta = 1$, whose blind testing results are shown in Fig. 3c. The same asymmetric behavior is observed for the trained P-D²NN, i.e., the output images in the forward direction are nearly identical to the demagnified versions of the input images, attaining a forward PCC of 0.979 and a forward diffraction efficiency of 1.06% (dashed lines in Fig. 3d), whereas the backward path only reaches a PCC of 0.525 and a diffraction efficiency of 0.43%, resulting in nearly dark output images. It is worth noting that the output images in both the forward and the backward directions, as depicted in Fig. 3c, are displayed with an identical range and the same color map. Although the forward and backward diffraction efficiencies, computed based on the total energy at their respective FOVs, might appear close, there is a substantial difference in the corresponding brightness of the forward/backward images due to the fact that the output images in the backward direction have much weaker average intensity per pixel (see Fig. 3c). In fact, Fig. 3d reveals that by varying the β value used in the training, the forward diffraction efficiency values of this unidirectional demagnifier P-D²NN design can be increased to $>45\%$ with a very good forward PCC value of >0.92 , while also suppressing the backward diffraction efficiency and backward PCC values to $\leq \sim 20\%$ and $< \sim 0.6$, respectively. Visualization of blind testing examples of the unidirectional demagnification P-D²NN designs trained with different β values can be found in Supplementary Fig. S2.

Comparison of P-D²NN performance against a regular D²NN architecture

Next, we compare the performance of the P-D²NN architecture against a regular D²NN structure for unidirectional magnification tasks. In this comparison, the P-D²NN model is directly taken from the unidirectional image magnification model trained with $\beta = 1$, as reported in Figs. 2b-c, which has a total of $N_b = 181,400$ diffractive features. The regular D²NN design employs uniformly sized diffractive layers, with the size of each layer equal to 270×270 pixels, yielding a total of $N = 2N_b$ trainable diffractive features. This standard D²NN design was trained using the same training loss functions (with $\beta = 1$), image datasets, and the number of epochs as we used for its pyramid counterpart shown in Figs.

2b-c. After its training, the blind inference was performed using the same test dataset of 1600 images to conduct the quantitative performance evaluations.

Figures 4a-b show the comparative blind testing results for the P-D²NN and the regular D²NN designs. In the forward direction, both diffractive networks demonstrate similar image magnification fidelity, as evident from both visual assessments and quantitative PCC values. Despite using ~2-fold smaller number of diffractive features in its design, P-D²NN outperforms the regular D²NN in terms of forward energy efficiency and energy suppression ratio, producing brighter forward output images and dimmer backward output images (see Fig. 4).

To further shed light on this comparison, we took the diffractive layers of the trained regular D²NN model and added light-blocking regions to each layer (Fig. 4c) with the sizes and the positions of the transmissive regions at each diffractive layer matching the corresponding layers in the P-D²NN design. This “trimmed” D²NN model, with only the central region of each diffractive participating in the inference process, has the same number of diffractive features as the P-D²NN (i.e., $N = N_b$) and was benchmarked using the same 1600-image test dataset. Naturally, the performance of this trimmed D²NN degrades compared to its original model, given that the peripheral diffractive neurons were disabled during the inference process. Moreover, when compared against the P-D²NN model, this trimmed D²NN produced inferior results across all image performance criteria (see Fig. 4c). This suggests that simply trimming a regular diffractive optical network to emulate the light propagation cone is not an effective approach.

To further investigate the influence of the diffractive layer dimensions on the performance of pyramid diffractive networks, we conducted additional analyses, where we adopted the P-D²NN delineated in Figs. 2b-c as our baseline model (also shown in Supplementary Fig. S3a). From this baseline, we incrementally enlarged the dimensions of each diffractive layer by m pixels, transforming, for instance, a 90×90 layer to $(90 + m) \times (90 + m)$, and a 270×270 layer to $(270 + m) \times (270 + m)$. For this analysis, we considered m values of 20, 40, and 70 (as illustrated in Supplementary Figs. S3b-d). Consequently, pyramid configurations with $N = 1.2N_b$, $N = 1.4N_b$, and $N = 1.8N_b$ were successively trained and quantitatively evaluated, with the results summarized in Supplementary Fig. S3. These analyses reveal that by infusing added degrees of freedom to a P-D²NN architecture, there is a modest unidirectional imaging performance improvement. Notably, in the case of $m = 70$ and $N = 1.8N_b$, P-D²NN outperforms the regular D²NN ($N = 2N_b$) in every quantitative performance metric, including higher PCC and diffraction efficiency in the forward direction. These findings further underscore the pyramid diffractive network configuration's architectural superiority for learning unidirectional image magnification (or demagnification) tasks.

Spectral response of the pyramid unidirectional magnification network

Next, we investigated the spectral behavior of the pyramid unidirectional magnifier depicted in Figs. 2b-c. This was done by taking the P-D²NN, initially trained at $\lambda_{\text{train}} = 0.75$ mm (Fig. 2b), and blindly testing it within a range of illumination wavelengths (λ_{test}) that diverge from the original training wavelength to assess its performance beyond the original training wavelength. Blind testing results for both the forward and backward paths across different λ_{test} values are shown in Fig. 5a. Notably, although the unidirectional magnifier P-D²NN was trained exclusively under a single illumination wavelength λ_{train} , it preserves its designed functionality to an extended spectral range, consistently achieving unidirectional image magnification in the forward path while suppressing the image formation in the reverse path.

We further evaluated the generalization of the trained unidirectional magnifier P-D²NN using a unique image dataset featuring resolution test targets with varying linewidths (Fig. 5b). The blind testing results at $\lambda_{\text{test}} = \lambda_{\text{train}}$ and $\lambda_{\text{test}} \neq \lambda_{\text{train}}$ validate the efficacy of P-D²NN in achieving a general-purpose unidirectional magnifier, even though it was exclusively trained on a different dataset. These analyses demonstrated that the trained P-D²NN unidirectional magnifier can resolve a minimum linewidth of approximately 6.3λ when working in the forward direction ($A \rightarrow B$), while effectively suppressing image formation in the reverse direction, $B \rightarrow A$.

A comprehensive quantitative analysis is also presented in Fig. 5c, summarizing the blind testing performance metrics evaluated within an illumination band covering from $\lambda_{\text{test}} = 0.6$ mm to $\lambda_{\text{test}} = 0.9$ mm. These quantitative results reveal that, when operating on the forward path, the unidirectional magnifier maintains a high PCC value of ≥ 0.82 within a spectral range of $[0.87\lambda_{\text{train}}, 1.17\lambda_{\text{train}}]$, i.e., within $[0.65$ mm, 0.88 mm]. Its forward diffraction efficiency remains fairly stable across the tested spectral range, with a value of $\geq 17.8\%$. In the reverse direction, on the other hand, the forward-backward energy ratio is maintained to be ≥ 20 (and ≥ 30) within a spectral range of $[0.89\lambda_{\text{train}}, 1.18\lambda_{\text{train}}]$ (and $[0.92\lambda_{\text{train}}, 1.11\lambda_{\text{train}}]$), respectively, demonstrating the broadband operation of this P-D²NN unidirectional magnifier design despite the fact that it was trained using a single illumination wavelength.

Wavelength-multiplexed P-D²NN design for unidirectional magnifier and demagnifier

As an even more challenging task, we integrated the functions of a diffractive unidirectional magnifier and a diffractive unidirectional demagnifier into the same P-D²NN, but in the opposite directions. The directionality of magnified or demagnified imaging is determined by the illumination wavelength, as depicted in Fig. 6a. At an illumination wavelength of λ_1 , the P-D²NN serves as a unidirectional *magnifier* in the forward direction, where the input images at FOV A are magnified at FOV B. Concurrently, the

image formation is inhibited at λ_1 in the backward path from FOV B to FOV A. In contrast, at an illumination wavelength of λ_2 , the image formation is inhibited in the forward path from FOV A to FOV B, while the image *demagnification* is achieved in the backward path, shrinking images from FOV B to FOV A. For this wavelength-multiplexed design, we set $\lambda_1 = 0.75$ mm and $\lambda_2 = 0.8$ mm, and incorporated the same set of training loss functions as described before for λ_1 and λ_2 separately (with $\beta = 1$; see the Methods section). Upon completion of the training, the P-D²NN model underwent blind testing using a test set composed of 1600 unique images (see Fig. 6b for some examples). These visual evaluations demonstrate that the wavelength-multiplexed P-D²NN simultaneously performs two distinct unidirectional image scaling operations in opposite directions, with the directionality of the unidirectional imaging determined by the illumination wavelength. In the forward path, the magnification function operates at λ_1 , but remains inactive at λ_2 . Conversely, in the backward path, the demagnification function operates at λ_2 but remains inactive at λ_1 (see Fig. 6b).

We further trained and tested four wavelength-multiplexed unidirectional P-D²NN models with different energy boosting factors, i.e., $\beta = 2.5, 3, 4,$ and 5 . The quantitative assessment of these different P-D²NN models is illustrated in Fig. 6c, showing the image *magnification* PCC and the diffraction efficiency in the forward direction ($A \rightarrow B$) for λ_1 , and the image *demagnification* PCC and the diffraction efficiency in the backward direction ($B \rightarrow A$) for λ_2 . These results indicate that tuning β values during the training of these wavelength-multiplexed P-D²NN diffractive networks can be used to adjust the trade-off between the image quality and diffraction efficiency, simultaneously applicable for the magnification and demagnification functions at both operating wavelengths (Fig. 6c).

Experimental demonstration of a unidirectional magnifier P-D²NN

We experimentally demonstrated our P-D²NN-based unidirectional magnifier design using monochromatic terahertz illumination at $\lambda = 0.75$ mm, as shown in Fig. 7a (also see the Methods section). For this experimental validation, we constructed a pyramid unidirectional magnifier consisting of three diffractive layers ($L_1, L_2,$ and L_3 in Fig. 7a), where each layer contains $40 \times 40, 60 \times 60,$ and 80×80 diffractive features along the forward direction, respectively. Each diffractive feature has a lateral size of $\sim 0.67\lambda$, selected based on the resolution of our 3D printer. The axial spacing between the consecutive layers, as well as between the diffractive layers and the input/output planes, is set to $\sim 13.3\lambda$. The pyramid network was trained to perform unidirectional image magnification with $M = 2$ in the forward direction. After the training was completed (see the Methods section for further details), the resulting diffractive layers were fabricated using 3D printing (Figs. 7b-c) and were assembled to form the physical unidirectional magnifier for the THz experimental test.

In our experiments, we tested the efficacy of the 3D-printed pyramid unidirectional magnifier in both the forward and backward directions using eight test objects, which were not part of the training data. The experimental results for both the forward and backward directions are shown in Fig. 7d, alongside their expected numerical results. It is demonstrated that the experimentally measured results in both the forward and backward directions show a good agreement with their numerical simulations. The 3D-printed unidirectional magnifier P-D²NN faithfully magnified the input objects in its forward direction while effectively inhibiting the image formation in the backward direction, aligning accurately with our numerical simulations.

Discussion

We presented a pyramid diffractive network architecture where the effective diffraction area scales in alignment with the geometrical scaling operation/task. Compared to conventional uniform-sized D²NN designs, P-D²NN learns unidirectional image scaling operations (magnification/demagnification) in a more efficient way by limiting its possible solution space to a confined region that is predetermined according to the behavior of ray optics. This allows the pyramid diffractive network architecture to converge to a more optimal solution, achieved with fewer diffractive degrees of freedom compared to regular D²NN designs, where each layer has the same number of diffractive features. In specific tasks, such as unidirectional image magnification, the optical energy is anticipated to transmit along a defined cone. As the input light diffracts through the P-D²NN layers, the majority of the energy remains confined within the areas delineated by geometrical optics. Allocating trainable diffractive features within these areas ensures a more effective energy utilization. We believe that this physics-inspired approach that integrates task specificity into the structure of the diffractive network layers can foster more efficient visual processors and more optimal task-specific diffractive networks.

Drawing further inspiration from the principles of pruning frequently used in conventional machine learning^{37,38}, where non-essential neurons are strategically pruned based on learned patterns, our presented P-D²NN approach can be further refined for various applications, such as spatial beam shaping and the design of reflective optical processors/components. Furthermore, instead of using a fixed architectural design for a given task, the diffractive layer placements and distributions can be incorporated as trainable parameters and dynamically tuned along with the optimization process. Such an advancement could redefine how diffractive optical networks are constructed, paving the way for task-specific designs that are not only more efficient but also inherently resilient across a spectrum of applications.

Methods

Numerical forward model of the diffractive optical network

The pyramid diffractive networks used in this work consist of a series of spatially structured surfaces designed by deep learning, each of which is considered as a thin optical element that modulates only the phase of the transmitted optical field. The transmission coefficient of the trainable diffractive neuron located at (x, y) position of the k^{th} diffractive layer, t^k , can be expressed as:

$$t^k(x, y) = \exp\{j\phi^k(x, y)\} \quad (1)$$

where $\phi^k(x, y)$ denotes the phase modulation of the diffractive neuron. Any two consecutive planes are connected to each other by free-space propagation, which is modeled using the angular spectrum approach¹⁰:

$$u(x, y, z + d) = \mathcal{F}^{-1}\{\mathcal{F}\{u(x, y, z)\} \cdot H(f_x, f_y; d)\} \quad (2)$$

where $u(x, y, z)$ is the original optical field, and $u(x, y, z + d)$ is the resulting field after propagation in free space for a distance of d along the optical axis. \mathcal{F} and \mathcal{F}^{-1} represent the 2D Fourier transform and 2D inverse Fourier transform operations, respectively. f_x and f_y represent the spatial frequencies along the x and y directions, respectively. $H(f_x, f_y; d)$ is the free-space transfer function, which is given by:

$$H(f_x, f_y; d) = \begin{cases} \exp\left\{jkd \sqrt{1 - \left(\frac{2\pi f_x}{k}\right)^2 - \left(\frac{2\pi f_y}{k}\right)^2}\right\}, & f_x^2 + f_y^2 < \frac{1}{\lambda^2} \\ 0, & f_x^2 + f_y^2 \geq \frac{1}{\lambda^2} \end{cases} \quad (3)$$

where λ is the illumination wavelength, $k = \frac{2\pi}{\lambda}$ and $j = \sqrt{-1}$.

By alternately applying the operations of free-space propagation (Eq. 2) and diffractive phase modulation (Eq. 1), the resulting complex field at the diffractive network's output can be obtained for a given optical field at the input FOV.

Digital implementation and training details

The diffractive network models used in our numerical simulations have a diffractive feature/neuron size of $\sim 0.53\lambda$, where $\lambda = 0.75$ mm. The pyramid network for unidirectional image magnification, as reported in Fig. 2, contains five diffractive layers with sequentially increasing numbers of trainable diffractive

features on each layer. From the first layer L_1 through the fifth layer L_5 , the diffractive layers progressively increased, with 90×90 , 140×140 , 180×180 , 220×220 , and 270×270 diffractive neurons at each layer respectively, leading to a total number of trainable neurons of $N = N_b = 181,400$. The magnification factor in the forward direction was selected as $M = 3$, with an input FOV comprising 90×90 pixels, and the output FOV having 270×270 pixels. The axial distance between any two consecutive planes was set as 40mm (i.e., 53.3λ). The weights of the loss terms used for training were chosen as: $\alpha = 8$, $\gamma = 1$, and $\mu = 2$, with β experimented across [0.5, 0.8, 1.0, 1.5, 2.0, 4.0] to generate the results reported in Fig. 2d and Supplementary Fig. S1.

The unidirectional demagnification pyramid network reported in Fig. 3 adopts a symmetric geometric arrangement with respect to its magnification counterpart (i.e., Fig. 2), in which the five diffractive layers have progressively decreasing numbers of trainable neurons as 270×270 , 220×220 , 180×180 , 140×140 , and 90×90 , respectively. The axial distance between any two consecutive planes was set as 40mm. The demagnification factor in the forward direction was selected as $D = 3$, with an input FOV comprising 270×270 pixels, and the output FOV having 90×90 pixels. The weights of the loss terms used for training were chosen as: $\alpha = 8$, $\gamma = 1$, and $\mu = 2$, with β experimented across [0.5, 1.0, 1.5, 2.0, 3.0, 4.0] to generate the results reported in Fig. 3d and Supplementary Fig. S2.

The 5-layer regular diffractive network reported in Fig. 4b is designed to achieve unidirectional magnification at a factor of $M = 3$. The input and output FOVs have 90×90 and 270×270 pixels, respectively. Each of the diffractive layers has 270×270 trainable neurons, summing up to $N = 2N_b$ trainable neurons across the structure. The axial separation between any two consecutive planes was also set as 40 mm ($\sim 53.3\lambda$). The weights in the training loss functions were selected as: $\alpha = 8$, $\beta = 1$, $\gamma = 1$, and $\mu = 2$ to be compared with its pyramid counterpart trained with the same set of weight parameters.

The wavelength-multiplexed diffractive network reported in Fig. 6 retains the same geometric architecture as Fig. 2. The two training wavelengths were selected as $\lambda_1 = 0.75$ mm and $\lambda_2 = 0.8$ mm. The weights in the training loss functions were also selected as: $\alpha = 8$, $\gamma = 1$, and $\mu = 2$, with β experimented across [1.0, 2.5, 3.0, 4.0, 5.0] to generate the results reported in Fig. 6c.

For the THz experimental verification, the pyramid diffractive network for unidirectional magnification has a diffractive feature size of 0.5 mm ($\sim 0.67\lambda$). The sampling period of the optical field was chosen as 0.25 mm ($\sim 0.33\lambda$) to ensure precise modeling. The diffractive network consists of three diffractive layers with 40×40 , 60×60 , and 80×80 diffractive neurons on each layer. The magnification factor in the forward direction was selected as $M = 2$, with input and output FOVs having the physical sizes of 15 mm

$\times 15$ mm and 30 mm $\times 30$ mm, respectively. The input and output FOVs are sampled into arrays of 10×10 pixels, with an individual pixel having a size of 1.5 mm and 3 mm (2λ and 4λ), respectively.

All the diffractive network models reported in the paper were trained with the QuickDraw dataset supplemented by a custom-created dataset comprising grating/fringe-like patterns with variance linewidths^{17,29}. The training data contains 200,000 images with 120,000 from the QuickDraw dataset and 80,000 from our customized dataset. The validation data contains 50,000 images with 30,000 from the QuickDraw dataset and 20,000 from our customized dataset. The blind testing data contains 1600 images with 1500 from the QuickDraw dataset and 100 from our customized dataset, without any overlap with the training or validation dataset. Each image was normalized to the range $[0, 1]$, followed by a set of random image transformations, including a rotation randomly selected from a range between -10° and $+10^\circ$, scaling with a factor sampled within $[0.9, 1.1]$, and a lateral shift in each direction, with values randomly drawn from $[-\lambda, +\lambda]$.

All the diffractive models in this study were trained and tested using PyTorch v1.13 with a GeForce RTX 3090 graphical processing unit (GPU, Nvidia Inc.). All the models were trained using the Adam optimizer³⁹ for 20 epochs with a learning rate of 0.03. The diffractive models designed under a single illumination wavelength for numerical analysis (e.g., Figs. 2-4) were trained with a batch size of 100. The training typically takes ~ 5 hours for 20 epochs. The diffractive model designed for wavelength-multiplexed operation (e.g., Fig. 6) was trained with a batch size of 50. The training takes ~ 9 hours for 20 epochs. The diffractive model for experimental demonstration (e.g., Fig. 7) was trained with a batch size of 200. The training takes ~ 0.5 hours for 20 epochs.

Experimental demonstration under THz radiation

Fig.7a and Supplementary Fig. S4 illustrate the schematic diagram of the experimental setup. The incident terahertz wave was generated by a modular amplifier (Virginia Diode Inc. WR9.0M SGX)/multiplier chain (Virginia Diode Inc. WR4.3x2 WR2.2x2) (AMC) with a compatible diagonal horn antenna (Virginia Diode Inc. WR2.2). A 10 dBm RF input signal at 11.1111 GHz (f_{RF1}) from the synthesizer (hp 8340B) was multiplied 36 times by the AMC to generate the output continuous-wave (CW) radiation at 0.4 THz. The AMC was modulated with a 1kHz square wave for lock-in detection. The object plane of the 3D-printed diffractive network was placed ~ 75 cm away from the exit aperture of the horn antenna. The distance is far enough to approximate the incident wave as a plane wave. The output plane of the diffractive network was 2D scanned with a 0.75 mm step size for an FOV of 30 mm $\times 30$ mm using a Mixer (Virginia Diode Inc. WRI 2.2) placed on an XY positioning stage built by vertically

combining two linear motorized stages (Thorlabs NRT100). A 10 dBm RF signal at 11.0833 GHz (f_{RF2}) was sent to the detector as a local oscillator to down-convert the signal to 1 GHz for further measurement. The down-converted signal was amplified by a low-noise amplifier (Mini-Circuits ZRL-1150-LN+) and filtered by a 1 GHz (± 10 MHz) bandpass filter (KL Electronics 3C40-1000/T10-O/O). The signal was first measured by a low-noise power detector (Mini-Circuits ZX47-60) and read by a lock-in amplifier (Stanford Research SR830) with the 1 kHz square wave as the reference signal. The raw data were calibrated into linear scale. A digital 4×4 binning was applied to the calibrated data to match the object feature size used in the numerical simulations.

Supplementary Information includes:

- Supplementary Figs. S1-S4
- Training loss functions
- Quantification metrics used for performance testing

References

1. Zhu, S. *et al.* Intelligent Computing: The Latest Advances, Challenges, and Future. *Intelligent Computing* **2**, 0006 (2023).
2. Mengü, D. *et al.* At the intersection of optics and deep learning: statistical inference, computing, and inverse design. *Adv. Opt. Photon., AOP* **14**, 209–290 (2022).
3. Wetzstein, G. *et al.* Inference in artificial intelligence with deep optics and photonics. *Nature* **588**, 39–47 (2020).
4. Sitzmann, V. *et al.* End-to-end optimization of optics and image processing for achromatic extended depth of field and super-resolution imaging. *ACM Transactions on Graphics* **37**, 1–13 (2018).
5. Côté, G., Côté, G., Lalonde, J.-F. & Thibault, S. Deep learning-enabled framework for automatic lens design starting point generation. *Opt. Express, OE* **29**, 3841–3854 (2021).
6. Wang, C., Chen, N. & Heidrich, W. dO: A Differentiable Engine for Deep Lens Design of Computational Imaging Systems. *IEEE Trans. Comput. Imaging* **8**, 905–916 (2022).
7. Li, Y., Qian, J., Feng, S., Chen, Q. & Zuo, C. Deep-learning-enabled dual-frequency composite fringe projection profilometry for single-shot absolute 3D shape measurement. *OEA* **5**, 210021–16 (2022).
8. Carolan, J. *et al.* Universal linear optics. *Science* **349**, 711–716 (2015).
9. Feldmann, J. *et al.* Parallel convolutional processing using an integrated photonic tensor core. *Nature* **589**, 52–58 (2021).
10. Lin, X. *et al.* All-optical machine learning using diffractive deep neural networks. *Science* **361**, 1004–1008 (2018).
11. Mengü, D., Luo, Y., Rivenson, Y. & Ozcan, A. Analysis of Diffractive Optical Neural Networks and Their Integration With Electronic Neural Networks. *IEEE Journal of Selected Topics in Quantum Electronics* **26**, 1–14 (2020).
12. Li, J., Mengü, D., Luo, Y., Rivenson, Y. & Ozcan, A. Class-specific differential detection in diffractive optical neural networks improves inference accuracy. *AP* **1**, 046001 (2019).

13. Rahman, M. S. S., Li, J., Mengü, D., Rivenson, Y. & Ozcan, A. Ensemble learning of diffractive optical networks. *Light Sci Appl* **10**, 14 (2021).
14. Li, J. *et al.* Spectrally encoded single-pixel machine vision using diffractive networks. *Science Advances* **7**, eabd7690 (2021).
15. Bai, B. *et al.* All-optical image classification through unknown random diffusers using a single-pixel diffractive network. *Light Sci Appl* **12**, 69 (2023).
16. Mengü, D. & Ozcan, A. All-Optical Phase Recovery: Diffractive Computing for Quantitative Phase Imaging. *Advanced Optical Materials* **10**, 2200281 (2022).
17. Shen, C.-Y., Li, J., Mengü, D. & Ozcan, A. Multispectral Quantitative Phase Imaging Using a Diffractive Optical Network. Preprint at <https://doi.org/10.48550/arXiv.2308.02952> (2023).
18. Rahman, M. S. S., Yang, X., Li, J., Bai, B. & Ozcan, A. Universal linear intensity transformations using spatially incoherent diffractive processors. *Light Sci Appl* **12**, 195 (2023).
19. Li, J. *et al.* Massively parallel universal linear transformations using a wavelength-multiplexed diffractive optical network. *AP* **5**, 016003 (2023).
20. Kulce, O., Mengü, D., Rivenson, Y. & Ozcan, A. All-optical synthesis of an arbitrary linear transformation using diffractive surfaces. *Light Sci Appl* **10**, 196 (2021).
21. Li, Y. *et al.* Universal Polarization Transformations: Spatial programming of polarization scattering matrices using a deep learning-designed diffractive polarization transformer. Preprint at <https://doi.org/10.48550/arXiv.2304.05724> (2023).
22. Bai, B. *et al.* Data-Class-Specific All-Optical Transformations and Encryption. *Advanced Materials* **35**, 2212091 (2023).
23. Bai, B. *et al.* To image, or not to image: class-specific diffractive cameras with all-optical erasure of undesired objects. *eLight* **2**, 14 (2022).
24. Mengü, D., Zhao, Y., Tabassum, A., Jarrahi, M. & Ozcan, A. Diffractive interconnects: all-optical permutation operation using diffractive networks. *Nanophotonics* (2022) doi:10.1515/nanoph-2022-0358.

25. Li, Y., Luo, Y., Mengu, D., Bai, B. & Ozcan, A. Quantitative phase imaging (QPI) through random diffusers using a diffractive optical network. *Light: Advanced Manufacturing* **4**, 1–16 (2023).
26. Luo, Y. *et al.* Computational imaging without a computer: seeing through random diffusers at the speed of light. *eLight* **2**, 4 (2022).
27. Li, J. *et al.* Unidirectional imaging using deep learning–designed materials. *Science Advances* **9**, eadg1505 (2023).
28. Mengu, D., Tabassum, A., Jarrahi, M. & Ozcan, A. Snapshot multispectral imaging using a diffractive optical network. *Light Sci Appl* **12**, 86 (2023).
29. Sakib Rahman, M. S. & Ozcan, A. Computer-Free, All-Optical Reconstruction of Holograms Using Diffractive Networks. *ACS Photonics* **8**, 3375–3384 (2021).
30. Huang, Z. *et al.* All-Optical Signal Processing of Vortex Beams with Diffractive Deep Neural Networks. *Phys. Rev. Appl.* **15**, 014037 (2021).
31. Zhu, H. H. *et al.* Space-efficient optical computing with an integrated chip diffractive neural network. *Nat Commun* **13**, 1044 (2022).
32. Goi, E., Schoenhardt, S. & Gu, M. Direct retrieval of Zernike-based pupil functions using integrated diffractive deep neural networks. *Nat Commun* **13**, 7531 (2022).
33. Liu, C. *et al.* A programmable diffractive deep neural network based on a digital-coding metasurface array. *Nat Electron* **5**, 113–122 (2022).
34. Luo, X. *et al.* Metasurface-enabled on-chip multiplexed diffractive neural networks in the visible. *Light Sci Appl* **11**, 158 (2022).
35. Benesty, J., Chen, J., Huang, Y. & Cohen, I. Pearson Correlation Coefficient. in *Noise Reduction in Speech Processing* vol. 2 1–4 (Springer Berlin Heidelberg, 2009).
36. Jongejan, J., Rowley, H., Kawashima, T., Kim, J. & Fox-Gieg, N. The quick, draw!-ai experiment. *Mount View, CA, accessed Feb* **17**, 4 (2016).
37. Liu, Z., Sun, M., Zhou, T., Huang, G. & Darrell, T. Rethinking the Value of Network Pruning. Preprint at <https://doi.org/10.48550/arXiv.1810.05270> (2019).

38. Safavian, S. R. & Landgrebe, D. A survey of decision tree classifier methodology. *IEEE Transactions on Systems, Man, and Cybernetics* **21**, 660–674 (1991).
39. Kingma, D. P. & Ba, J. Adam: A Method for Stochastic Optimization. *arXiv:1412.6980 [cs]* (2017).

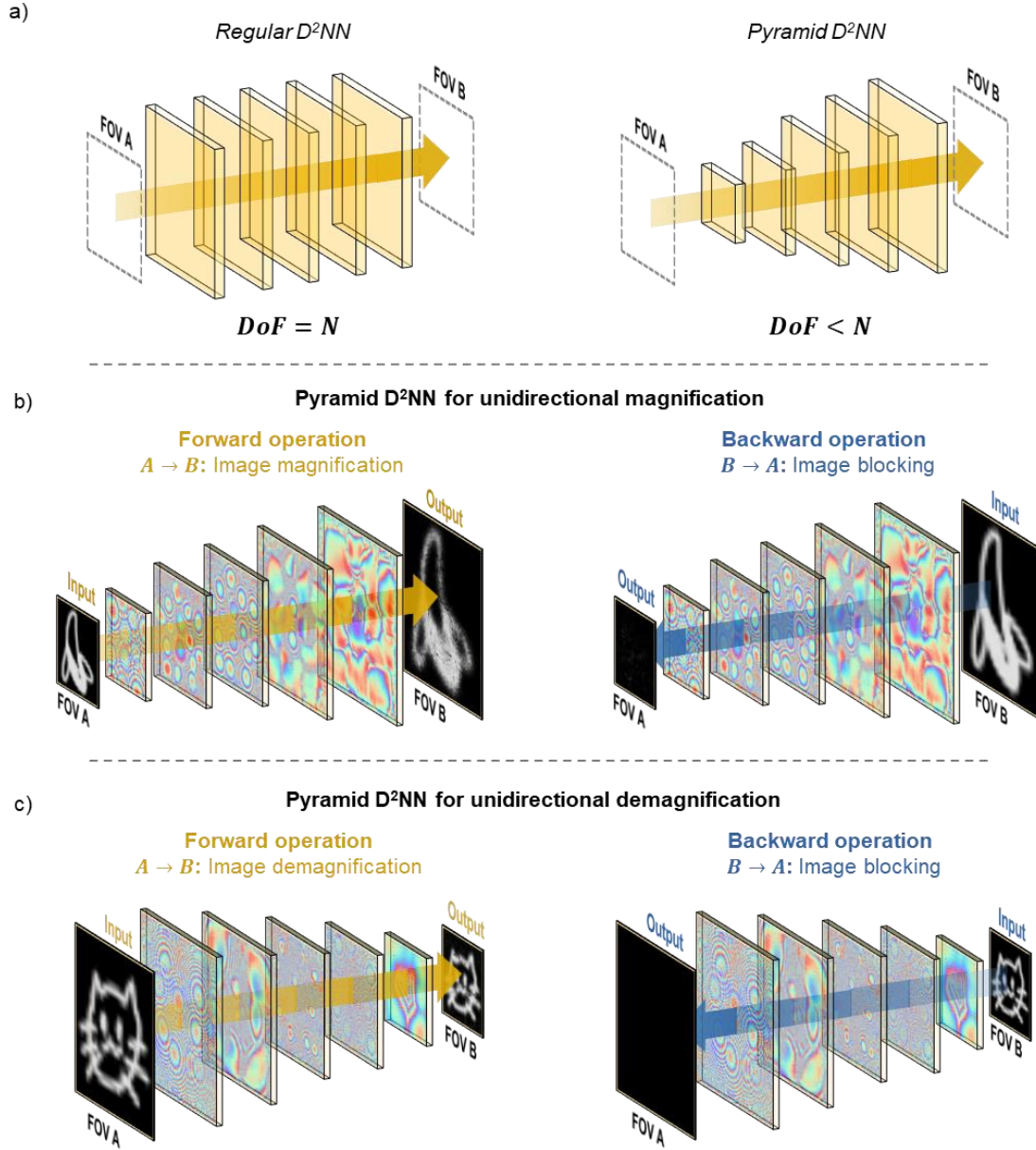


Figure 1. Schematic of pyramid diffractive networks in unidirectional magnification and demagnification. (a) Comparison of a conventional regular D^2NN and a pyramid D^2NN , where the P- D^2NN has smaller degrees-of-freedom (DoF, i.e., the number of independent diffractive features) than the regular D^2NN . (b) Pyramid diffractive network for unidirectional image magnification. The network performs image magnification in the forward direction ($A \rightarrow B$) and image blocking in the opposite direction ($B \rightarrow A$). (c) Pyramid diffractive network for unidirectional image demagnification. The network performs image demagnification in the forward direction ($A \rightarrow B$) and image blocking in the opposite direction ($B \rightarrow A$).

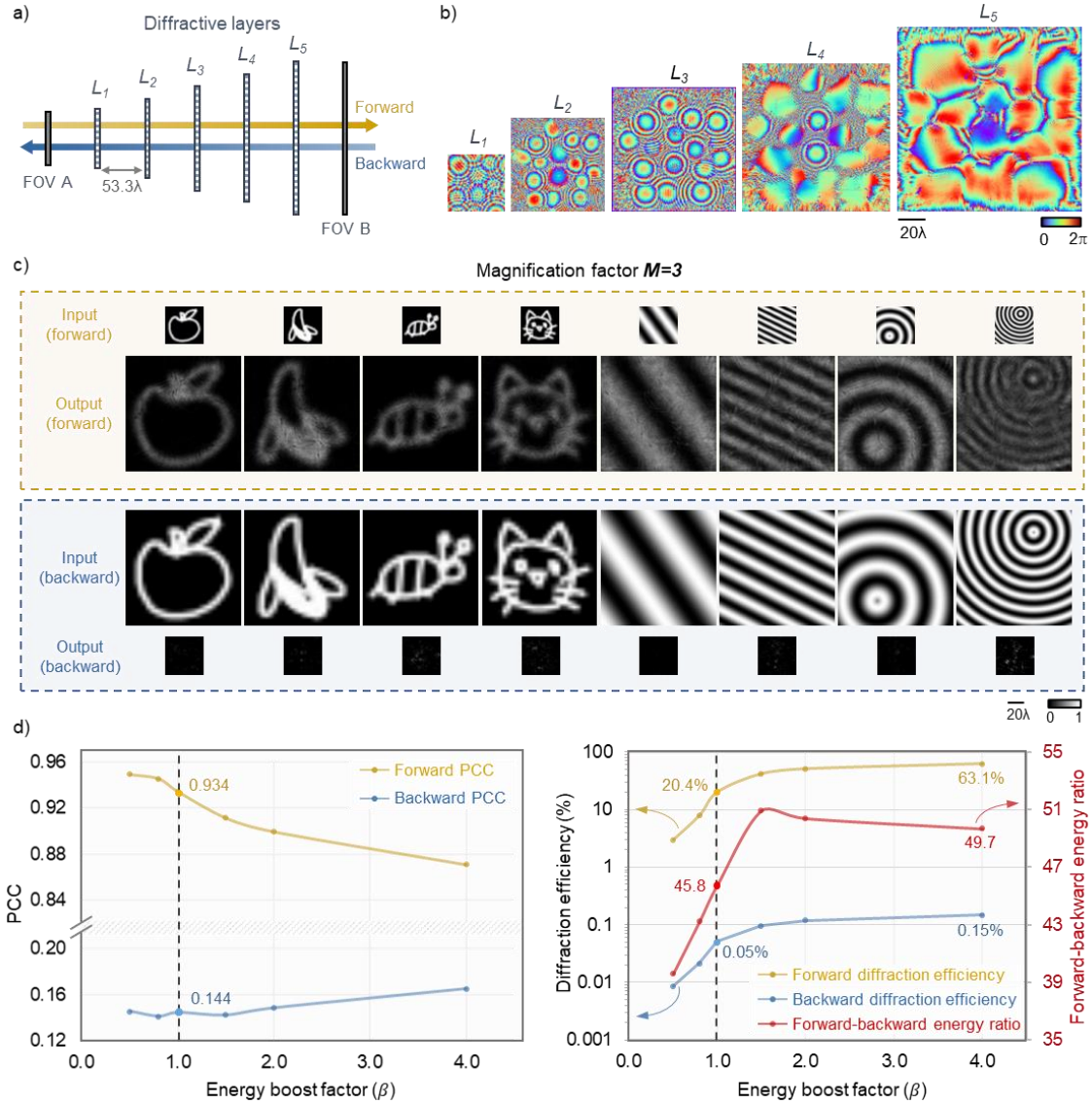


Figure 2. Design schematic and blind testing results of the pyramid unidirectional magnifier. (a) Layout of a five-layer pyramid diffractive network for unidirectional image magnification. (b) The resulting diffractive layers after deep learning-based optimization (with energy boost factor $\beta = 1$). (c) Examples of blind testing results of the trained unidirectional magnifier in both the forward and backward directions (with energy boost factor $\beta = 1$). (d) Quantitative evaluations of the unidirectional magnifiers trained with varying β values.

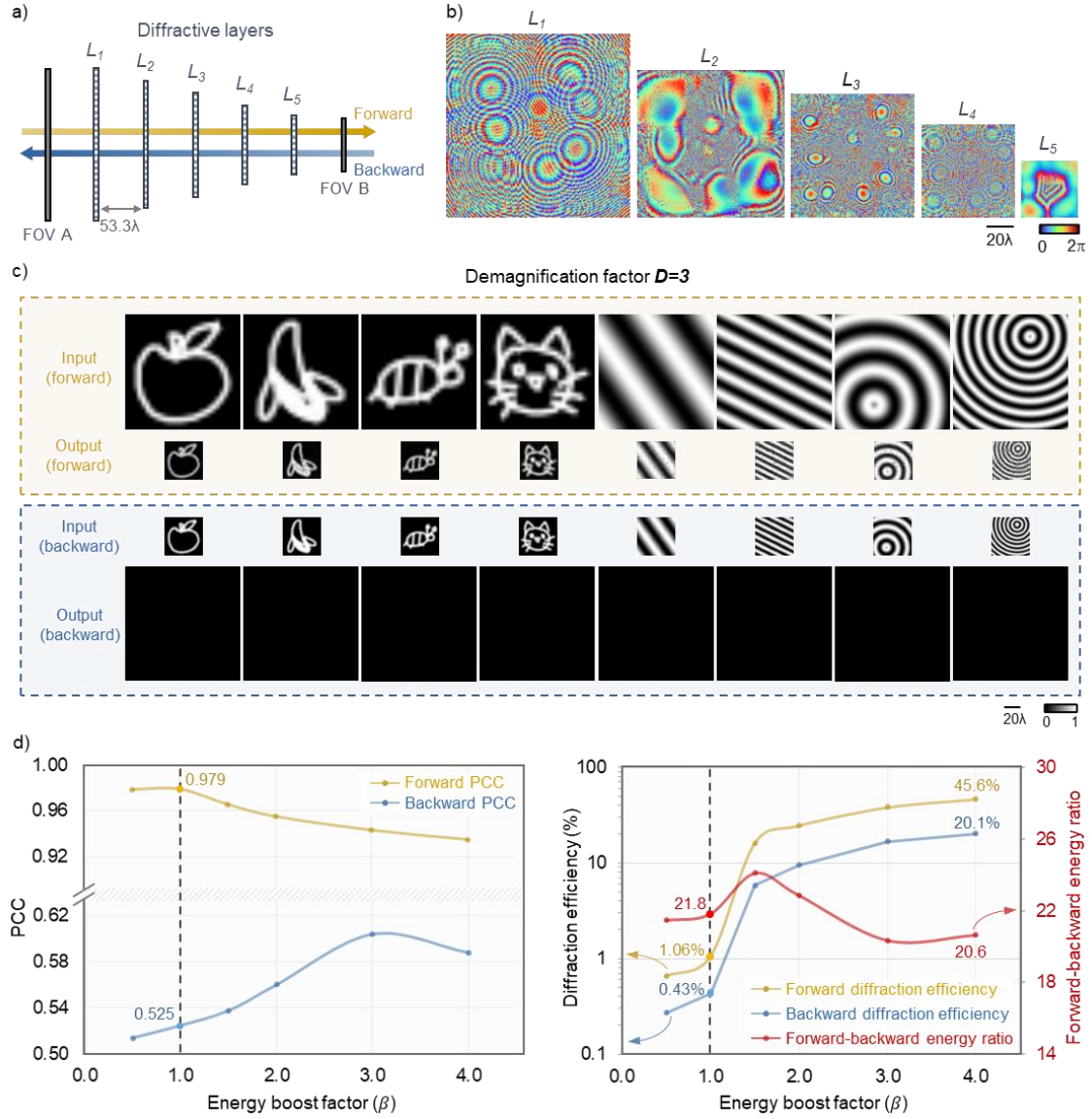


Figure 3. Design schematic and blind testing results of the pyramid unidirectional demagnifier. (a) Layout of a five-layer pyramid diffractive network for unidirectional image demagnification. (b) The resulting diffractive layers after deep learning-based optimization (with energy boost factor $\beta = 1$). (c) Examples of blind testing results of the trained unidirectional demagnifier in both the forward and backward directions (with energy boost factor $\beta = 1$). (d) Quantitative evaluations of the unidirectional demagnifiers trained with various β values.

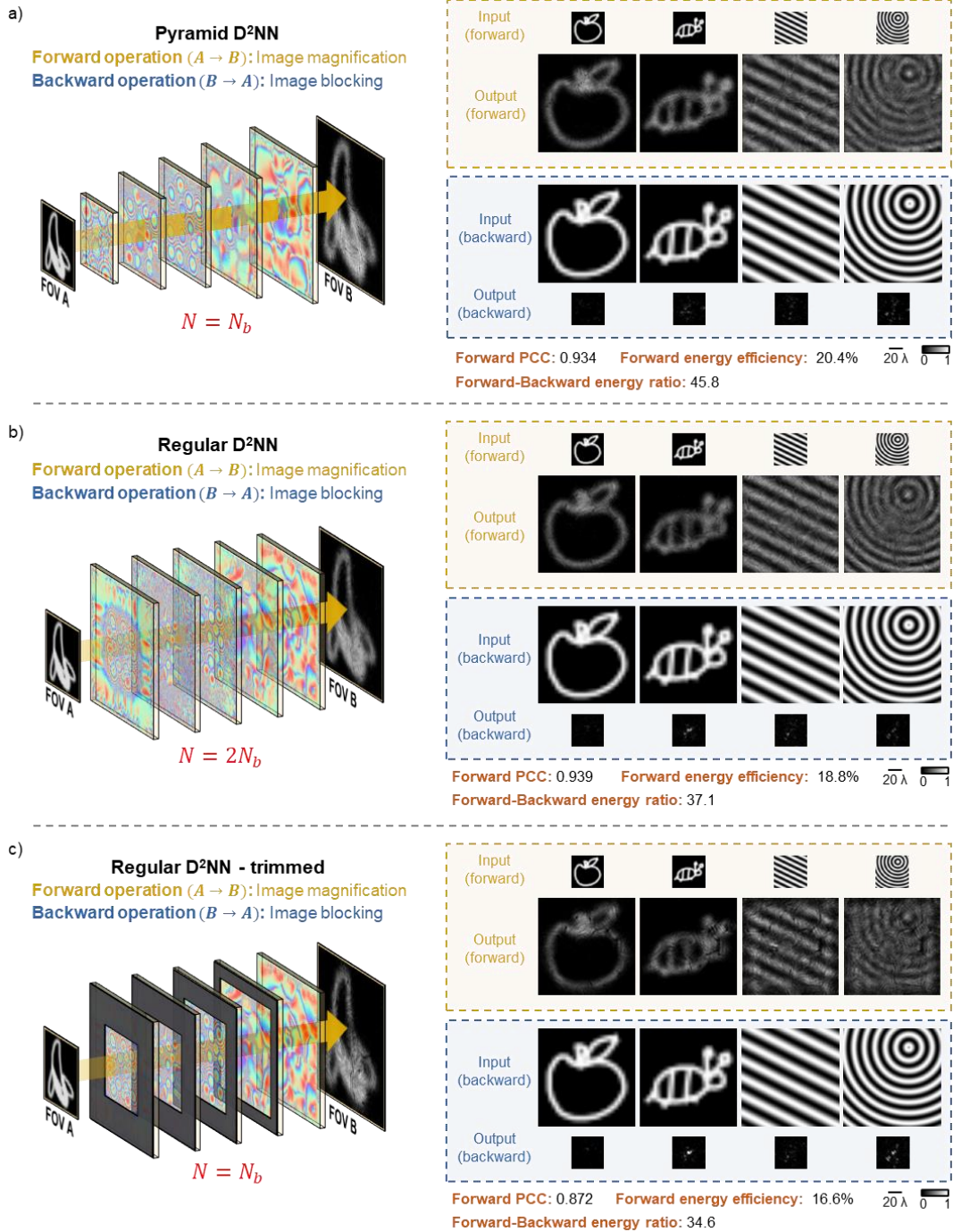


Figure 4. Comparison of the pyramid-structured D²NN against the regular uniform-sized D²NN. (a) Design layout and blind testing results of a P-D²NN-based unidirectional magnifier, where the P-D²NN has $N = N_b$ diffractive features. (b) Design layout and blind testing results of a regular D²NN-based unidirectional magnifier, where the regular D²NN has $N = 2N_b$ diffractive features. (c) Design layout and blind testing results of a trimmed version of the regular D²NN, where the trimmed D²NN has $N = N_b$ diffractive features. The trimmed D²NN was obtained by taking the diffractive layers of the trained regular D²NN (depicted in (b)) and adding light-blocking regions to match the transmissive regions of the P-D²NN (depicted in (a)).

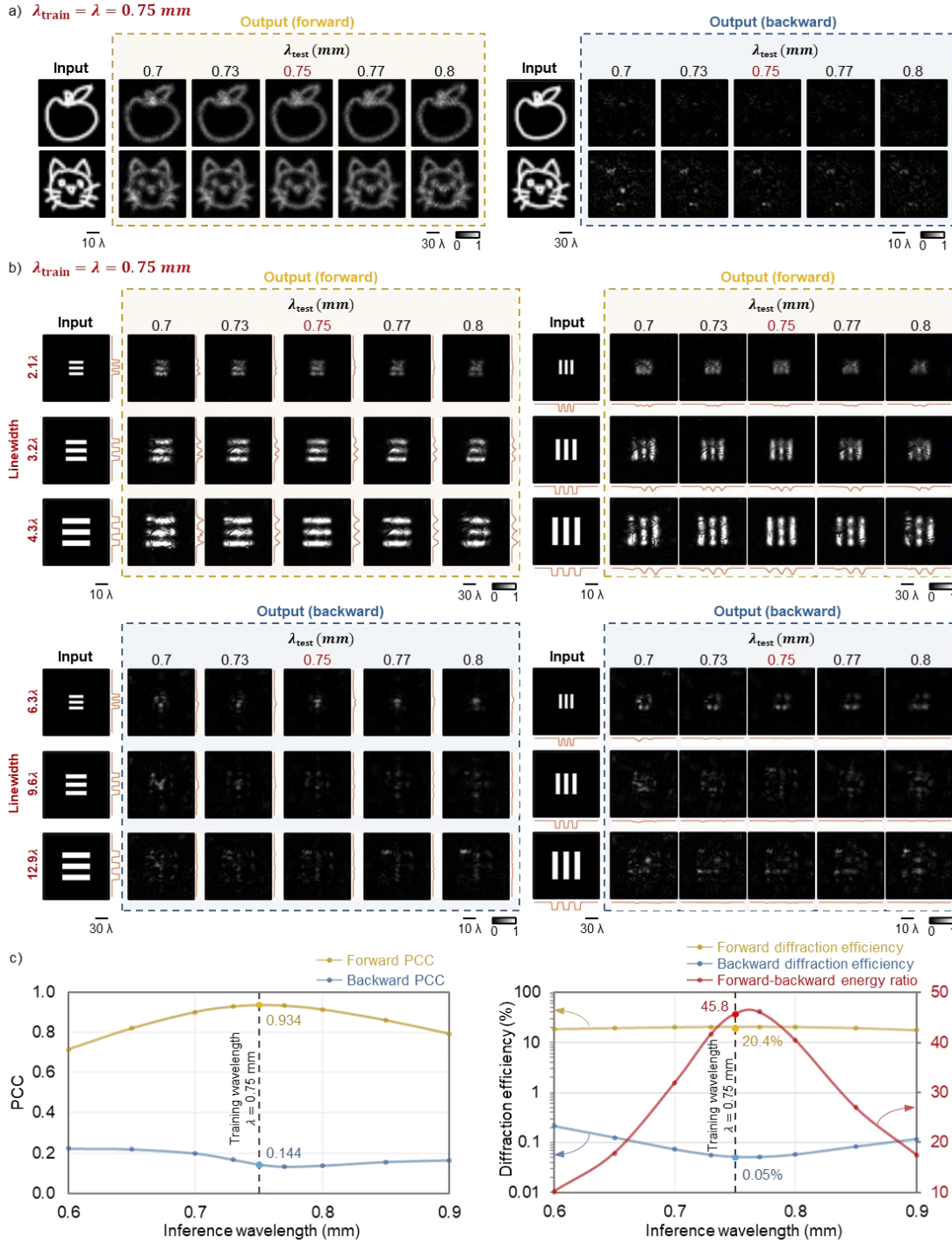


Figure 5. Spectral behavior of the pyramid unidirectional magnifier. (a) Blind inference results of the unidirectional magnifier design shown in Figs. 2b-c under different illumination wavelengths. (b) Blind inference results of the unidirectional magnifier design shown in Figs. 2b-c at different illumination wavelengths using customized resolution target images, demonstrating its generalization capability to new types of images. (c) Quantitative evaluation results of the unidirectional magnifier shown in Figs. 2b-c blindly tested at different illumination wavelengths

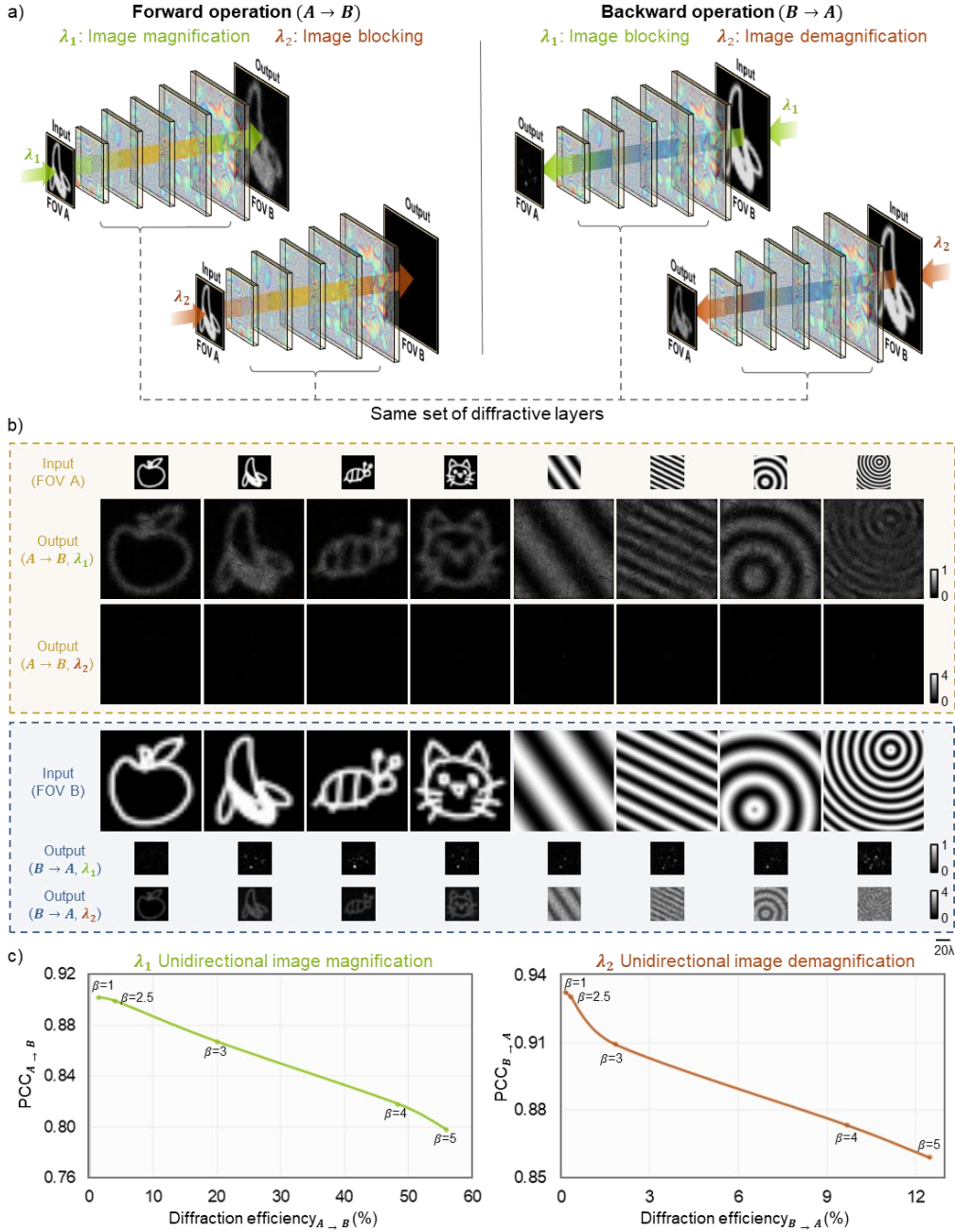


Figure 6. Demonstration of the wavelength-multiplexed P-D²NN performing unidirectional magnification and unidirectional demagnification tasks simultaneously at two distinct incident wavelengths. (a) The design concept of the wavelength-multiplexed pyramid diffractive network. At wavelength λ_1 , the network performs image magnification in its forward direction ($A \rightarrow B$) and image blocking in its backward direction ($B \rightarrow A$). Oppositely, at wavelength λ_2 , the network performs image blocking in its forward direction ($A \rightarrow B$) and image demagnification in its backward direction ($B \rightarrow A$). (b) Examples of blind testing results of the wavelength-multiplexed P-D²NN in both the forward and backward directions at two distinct design wavelengths. (c) Quantitative evaluations of the wavelength-multiplexed P-D²NN trained under different β values, showing the trade-off between image magnification/demagnification fidelity and the corresponding diffraction efficiency along the same direction.

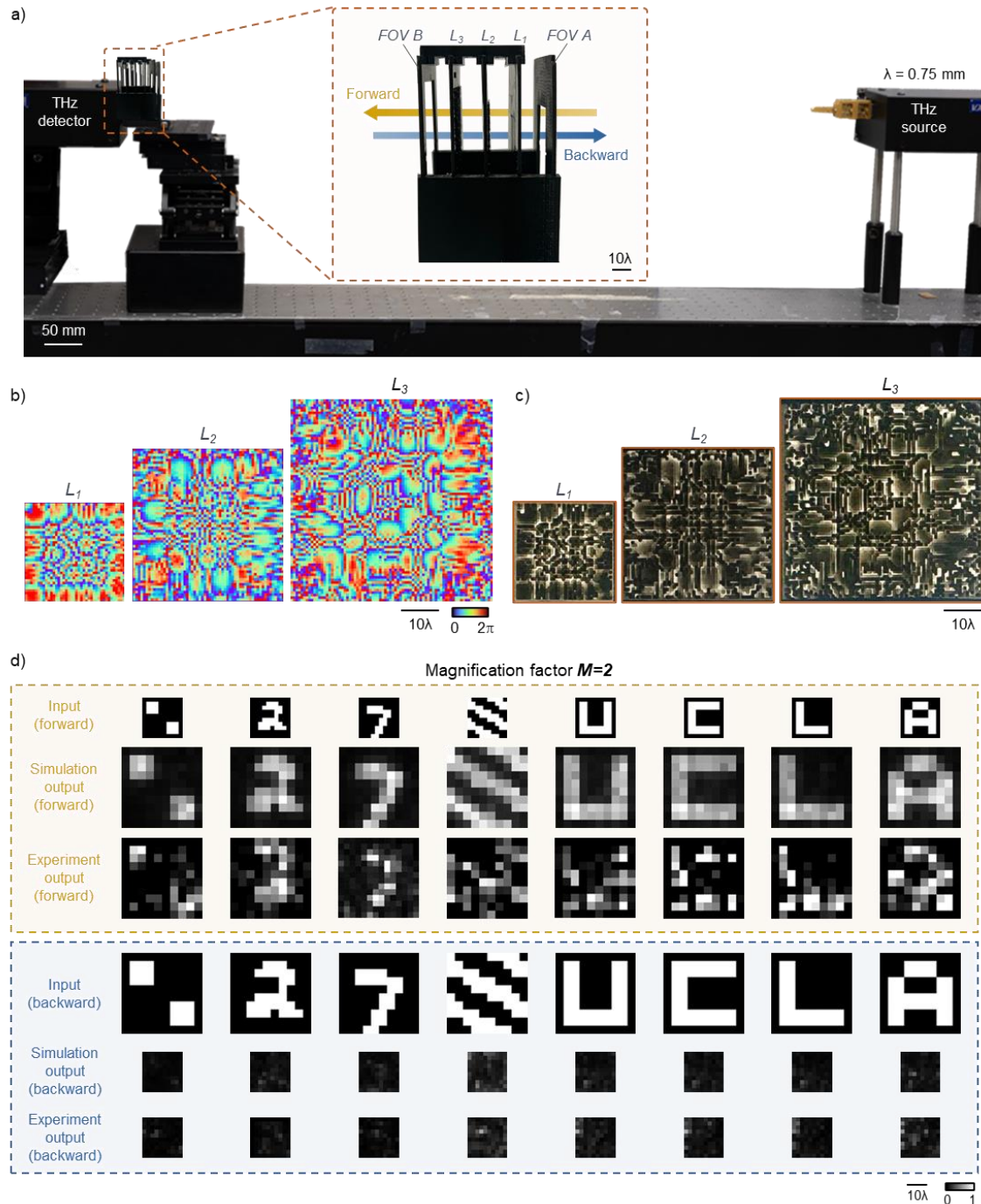


Figure 7. Experimental demonstration of the unidirectional magnifier using a pyramid diffractive network. (a) Photographs of the fabricated P-D²NN and the experimental setup with $\lambda = 0.75$ mm THz illumination. (b) The converged phase patterns of the diffractive layers. (c) Photographs of the 3D printed diffractive layers. (d) Experimental testing results of the unidirectional magnifier using a pyramid diffractive network.